Parametric Dictionary Learning for Sparsity-Based TWRI in Multipath Environments

Michael Leigsnering, *Student Member, IEEE,*
Fauzia Ahmad, *Senior Member, IEEE,* Moeness G. Amin, *Fellow, IEEE,*
and Abdelhak M. Zoubir, *Fellow, IEEE*

Abstract

Sparsity-based multipath exploitation is a promising method to eliminate ghost targets in through-the-wall radar images and utilize the additional energy in secondary reflections. The applicability of existing methods, however, is limited due to the assumption of perfectly known geometry of building interiors. We develop a parametrized multipath signal model that captures unknown or partially known wall locations. This model is used in the proposed joint image reconstruction and wall position estimation method. In order to further improve practicability in realistic scenarios, a reconstruction method based on deployment of multiple small aperture radar modules is discussed. To this end, we analyze theoretical performance bounds for co-located and distributed placements of the various modules. Supporting results based on simulated and experimental lab data are provided.

Index Terms

Compressive sensing (CS), sparse reconstruction, multipath exploitation, through-the-wall radar imaging (TWRI), wall uncertainties, distributed, co-located.

The work by F. Ahmad and M. G. Amin was supported by ARO and ARL under contract W911NF-11-1-0536.

M. Leigsnering and A. M. Zoubir are with the Signal Processing Group, Institute of Telecommunications, Technische Universität Darmstadt, 64283 Darmstadt, Germany (e-mail: leigsnering@spg.tu-darmstadt.de; zoubir@spg.tu-darmstadt.de).

F. Ahmad and M. G. Amin are with the Radar Imaging Laboratory, Center for Advanced Communications, Villanova University, Villanova, PA 19085 USA (e-mail: fauzia.ahmad@villavova.edu; moeness.amin@villanova.edu).

I. INTRODUCTION

The ability to "see" through walls or visually opaque obstacles may be obtained via through-the-wall radar imaging (TWRI). This emerging technology applies the radar principle, i.e., transmitting and receiving electromagnetic (EM) waves to reveal the location of behind-the-wall objects. Due to the numerous applications in firefighting, search and rescue, and police missions as well as for situational awareness in urban areas, it has received much research interest in the recent decade [1]–[9].

With much progress made in this area over the last decade, one of the remaining challenges in TWRI is dealing effectively with the high amount of multipath in indoor environments [10], [11]. The EM wave does not only propagate along the shortest path between the antenna and the target, but may also travel on various indirect paths. These indirect paths mainly arise due to secondary reflections at interior building walls, floor, and ceiling. In the image formation process, multipath propagation leads to the appearance of ''ghost" targets, which are energy accumulations at locations that do not correspond to true targets in the scene. The rich indoor multipath environment has been primarily seen as a nuisance in TWRI, as it clutters the reconstructed scene and renders interpretation difficult. However, multipath returns can potentially be utilized to provide more information about the target [12]–[14].

Multipath exploitation in radar imaging was proposed by Kidera et al. [15] to reveal shadowed parts of a scene. This idea has also been applied to the removal and exploitation of multipath ghosts in TWRI in [12]. Making use of the sparsity in typical TWRI and urban sensing scenes, ghost-free images were reconstructed using multipath exploitation within the compressive sensing (CS) framework in [14], [16], [17]. However, these multipath exploitation methods leverage prior information of the indoor/urban scattering environment to remove the ghost targets and improve the image quality. Inaccurate knowledge of interior building layout and the room geometry can lead to severe impairments in the effectiveness of such multipath exploitation approaches. In ground-based surveillance, the image impairments would depend on the employed physical or synthetic aperture as well as whether EM sensing is performed using co-located or distributed radar system configurations. Both configurations can be defined using man-portable radar modules equipped with a limited number of transmitters and receivers. Such a modular approach is emerging as an effective and flexible alternative to vehicle-mounted systems.

In this paper, we perform joint exploitation of the multipath returns and the sparsity of the behind-the-wall scene for a modular multistatic radar system comprising several man-portable TWRI modules. Both co-located and distributed configurations are considered. We assume that the radar modules cooperate with each other and their measurements are combined in a central processing station. We consider stationary targets and assume that the front wall reflections have been mitigated. The received signal model and the reconstruction problem is formulated such that the combined measurements can be fully utilized to form an image. In contrast to the co-located case, the measurements from a distributed setup need to be combined in a non-coherent manner as the target reflectvity usually changes with aspect and bistatic angles. To this end, we extend the group sparse reconstruction approach for multipath exploitation, originally proposed in [14], to exploit the structure in the sparse solution of the image reconstruction problem for the co-located and distributed configurations. The dictionaries for both configurations are analyzed analytically to predict the reconstruction performance. Further, we propose a parametrization of the wall locations in the signal model to accommodate uncertainties in the knowledge of the scattering environment. This leads to a joint optimization problem to simultaneously solve for the wall locations and perform a ghost-free scene reconstruction at the central processing station. However, the optimization problem is highly non-linear and non-convex in the wall parameters. This is addressed by adopting a nested approach, wherein the convex scene reconstruction problem is solved for fixed wall locations in an interactive fashion, with the wall locations updated at each step. We investigate various non-linear and non-convex optimization methods and evaluate their performance using numerical simulations and measured data from a semi-controlled lab experiment.

The main contributions of this paper can be summarized as follows:

- We propose a modular approach for TWRI using man-portable small aperture radar modules and analyze the corresponding dictionaries in terms of their impact on sparse reconstruction performance.
- A parametric approach to sparse reconstruction in the presence of multipath propagation and wall location uncertainties is proposed for both distributed and co-located configurations. Various methods for solving the joint non-convex optimization problem are evaluated.

It is noted that the proposed multipath exploitation approach in the presence of wall location

uncertainties is also applicable to translational motion via change detection imaging. In this case, by coherently subtracting two sets of measurements taken at different time instants, the equivalent stationary scene would depict the initial and final positions of targets in the image. The sudden partial motion of a large scatterer, e.g. the human torso and limbs, also has an equivalent stationary scene that was modeled and sparsely reconstructed in [18]. Further, related sparsity based concepts have been used to estimate deviations in the flight path for improved motion correction in airborne synthetic aperture radar (SAR) imaging [19]–[21]. Airborne SAR faces a similar problem, as images become de-focused if uncertainties in the platform motion exist. Ohnon and Cetin [19] treat these uncertainties as phase errors and propose a joint sparsity-based SAR imaging and phase error correction method. Wei *et al.* [20] model the platform position errors in azimuth and propose an iterative scheme that estimates the position errors and obtains a CS reconstruction of the SAR image. Yang *et al.* [21] model platform position errors in all directions and propose a sparsity-based method to jointly recover the motion errors and the SAR image. Compressive sensing (CS) in the context of multiple-input multiple-output air surveillance radar has been studied for the co-located and distributed cases in [22], [23]. Therein, efficient sparse reconstruction method are proposed to reconstruct the targets using a co-located [22] and distributed [23] radar configuration, however, no multipath effects or uncertainties in the array locations are considered. To the best of our knowledge, multipath modeling and exploitation in sparse image reconstruction both with and without wall location uncertainties using small aperture modular systems has not been addressed in prior works in the context of TWRI.

The remainder of the paper is organized as follows. In Section II, we discuss the multipath signal models for co-located and distributed placements of the radar modules. Furthermore, the resulting dictionaries are analyzed to establish theoretical performance bounds on the sparse scene reconstruction. In Section III, we propose sparse reconstruction approaches for co-located and distributed TWRI systems. These are combined with a method to jointly estimate interior wall locations and reconstruct the scene in order to deal with wall position uncertainties. The effectiveness of the proposed algorithms is demonstrated using simulated and measured data in Sections IV, respectively. We conclude the paper in Section V.

Notations: We use lower-case (upper-case) bold characters to denote vectors (matrices). $(\cdot)^T$ and $(\cdot)^H$, respectively, denote the transpose and conjugate transpose of a matrix or vector, whereas $\mathrm{diag}(\cdot)$ and $\mathrm{blkdiag}(\cdot)$ represent a diagonal matrix and a block diagonal matrix, respectively.

$\|\cdot\|_2$ and $\|\cdot\|_{1,2}$, respectively, denote the Euclidean and mixed ℓ_1-ℓ_2 norms. In the context of compressive sensing, $\bar{\boldsymbol{z}}$ is a measurement vector, $\boldsymbol{\Phi}$ represents a measurement or downsampling matrix, $\boldsymbol{\Psi}$ denotes a dictionary, and $\boldsymbol{\sigma}$ is the unknown sparse vector of interest, i.e., the image. Moreover, we define the sensing matrix $\boldsymbol{A} = \boldsymbol{\Phi}\boldsymbol{\Psi}$.

II. Signal Model

We establish a multistatic pulsed radar model with different transmit and receive arrays. We assume a modular concept, i.e. the transmit and receive arrays consist of several sub-arrays. Thus, each radar module has a limited number of transmitters and receivers that operate fully coherently. The measurements from all modules are communicated to a central processing unit where they are fused to reconstruct the scene being interrogated. The radar modules may be deployed such that sensing through walls is performed based on co-located or distributed aperture configurations. In the co-located case, the modules are closely-spaced so that the target is viewed with the same aspect angle and the measurements from the various modules can be combined coherently. On the other hand, in the distributed case, the modules are placed distant apart and the targets' aspect angles may vary widely across the modules. Therefore, a coherent combination of the measurements from the various modules is no longer feasible. In the sequel, we first describe the measurement model for a single module and then extend it to multiple radar modules.

A. Signal Model Based on a Single Module

Each module consists of an M-element transmit array and an N-element receive array. We assume a sequential operation of the transmitters, i.e. the waveforms are orthogonal by virtue of time multiplexing.

Let the two-dimensional (2-D) scene of interest be discretized into a uniform grid of P points, with $\boldsymbol{x}_p = (x_p, y_p), p = 0, \ldots, P-1$ being the position of the pth grid point. The complex reflectivity associated with the pth grid point is denoted by σ_p, with $\sigma_p = 0$ representing the absence of a point target at the pth grid point. With a small number of targets, only a few of the grid points assume non-zero values. The transmitted wideband pulse is expressed as $\Re\{s(t)\exp(j2\pi f_c t)\}$, where t is the fast time, $s(t)$ is the pulse in the complex baseband, and f_c is the carrier frequency. The sequential operation of the M transmitters results in a temporal spacing of integer multiples of T_r between their pulses. Neglecting the front wall returns and

the multipath contributions, the received signal corresponding to transmitter $m = 0, \ldots, M-1$ and receiver $n = 0, \ldots, N-1$ is given by

$$z_{mn}(t) = \sum_{p=0}^{P-1} \sigma_p s\left(t - mT_r - \tau_{pmn}\right) e^{-j2\pi f_c (mT_r + \tau_{pmn})}, \tag{1}$$

where τ_{pmn} is the bistatic propagation delay from the mth transmitter to the pth target and back to the nth receiver. The received signal $z_{mn}(t)$ is sampled uniformly at N_T time steps with sampling interval T resulting in an $N_T \times 1$ vector $\boldsymbol{z}_{mn}$. The sampling interval is chosen to attain the Nyquist rate of the wideband pulse $s(t)$. After discretization and vectorization of (1), we obtain

$$\boldsymbol{z} = \boldsymbol{\Psi}^{(0)} \boldsymbol{\sigma}^{(0)}, \tag{2}$$

where $\boldsymbol{z}$ is the result of stacking the received signal vectors $\{\boldsymbol{z}_{mn}, m = 0, \ldots, M-1, n = 0, \ldots, N-1\}$ and $\boldsymbol{\sigma}^{(0)} = [\sigma_0, \ldots, \sigma_{P-1}]^T$. The direct path dictionary $\boldsymbol{\Psi}^{(0)}$ is defined as

$$\left[\boldsymbol{\Psi}^{(0)}\right]_{i+nN_T+mN_TN,p} = s\left(t_i - mT_r - \tau_{pmn}\right) e^{-j2\pi f_c (mT_r + \tau_{pmn})}, \tag{3}$$

where $i = 0, \ldots, N_T - 1, m = 0, \ldots, M-1, n = 0, \ldots, N-1, p = 0, \ldots, P-1$.

Whereas the front wall contribution may be removed by a suitable wall clutter mitigation method [24]–[26], the multipath contribution should be properly modeled. We employ the geometric optics multipath model from [14], [27] in order to describe the received multipath returns. We restrict ourselves to multipath originating from secondary scattering at interior walls. The wall locations are parametrized as prior knowledge of exact wall locations is usually not available. Modeling $R-1$ additive multipath contributions in the received signal, we obtain

$$\boldsymbol{z} = \boldsymbol{\Psi}^{(0)} \boldsymbol{\sigma}^{(0)} + \boldsymbol{\Psi}^{(1)}(\boldsymbol{w}) \boldsymbol{\sigma}^{(1)} + \cdots + \boldsymbol{\Psi}^{(R-1)}(\boldsymbol{w}) \boldsymbol{\sigma}^{(R-1)}, \tag{4}$$

where $\boldsymbol{\Psi}^{(r)}(\boldsymbol{w}), r = 1, \ldots, R-1$ are the dictionaries under multipath propagation, $\boldsymbol{w}$ is the vector of wall positions, and $\boldsymbol{\sigma}^{(r)}$ is the reflectivity vector or sub-image for the rth path. The multipath dictionaries $\boldsymbol{\Psi}^{(r)}(\boldsymbol{w})$ can be calculated using (3), with τ_{pmn} replaced by the corresponding path and wall location dependent propagation delays $\tau^{(r)}_{pmn}(\boldsymbol{w})$. The propagation delays for indirect paths involving secondary reflections at interior walls can be calculated using the image source principle [14]. That is, the indirect path can be reflected about the interior wall, yielding an alternative antenna-target geometry involving a virtual target, as shown in Fig. xx. The delay

associated with the indirect path is the same as that of the path from the virtual target to the antenna.

We assume a rectangular room aligned with the coordinate system; hence, the location of each wall can be described by a single parameter. That is, downrange coordinates specify the locations of walls parallel to the horizontal axis, whereas crossrange coordinates are sufficient for walls that are perpendicular to the horizontal axis. In a typical scenario, $\boldsymbol{w}$ contains three elements corresponding to the crossrange or downrange positions of the two side walls and the back wall enclosing the room. Note that a path and, thus, the corresponding dictionary are only affected by an element in $\boldsymbol{w}$ if the path involves secondary scattering at the respective interior wall. As the target scattering occurs under different aspect or bistatic angles, the radar cross section (RCS) may change from one path to another. Further, any additional losses on the multipath can be absorbed into the respective reflectivity vector. For a more detailed treatment of how to obtain the multipath model, refer to [14], [27]. Finally, we stack all sub-images in a $PR \times 1$ vector $\tilde{\boldsymbol{\sigma}} = \left[\left(\boldsymbol{\sigma}^{(0)}\right)^T \left(\boldsymbol{\sigma}^{(1)}\right)^T \cdots \left(\boldsymbol{\sigma}^{(R-1)}\right)^T\right]^T$ and concatenate the dictionaries corresponding to the R paths to form a composite dictionary $\tilde{\boldsymbol{\Psi}}(\boldsymbol{w}) = [\boldsymbol{\Psi}^{(0)}\ \boldsymbol{\Psi}^{(1)}(\boldsymbol{w})\ \cdots\ \boldsymbol{\Psi}^{(R-1)}(\boldsymbol{w})] \in \mathbb{C}^{N_T MN \times PR}$, resulting in

$$\bar{\boldsymbol{z}} = \boldsymbol{\Phi}\boldsymbol{z} + \bar{\boldsymbol{n}} = \boldsymbol{\Phi}\tilde{\boldsymbol{\Psi}}(\boldsymbol{w})\tilde{\boldsymbol{\sigma}} + \bar{\boldsymbol{n}}, \tag{5}$$

where $\boldsymbol{\Phi}$ represents a possible downsampling operation, and $\bar{\boldsymbol{n}}$ is the measurement noise vector, which is typically modeled as complex circular Gaussian. A common choice for $\boldsymbol{\Phi}$ is a random mixing scheme in the time domain and/or skipping array elements in the spatial domain [28], [29]. If no downsampling in time or space is desired, $\boldsymbol{\Phi}$ can be set as the identity matrix.

Note that the model is linear in the unknown reflectivity vector. However, it is non-linear in the unknown wall positions.

B. Signal Model Based on Multiple Radar Modules

Consider the case where a number S of the above described multistatic pulsed radar modules are deployed. Each transmitted pulse is assumed to be received simultaneously by all receivers from all units. Hence, the total number of measurements is increased S^2-fold. Two cases can be distinguished, namely, the co-located and the distributed configurations. In the co-located configuration, the modules are positioned next to each other at the same standoff distance from

the front wall, emulating a multistatic radar system with much longer transmit and receive array apertures. The resulting system views the scene approximately from the same angle, thereby permitting the RCS changes to be neglected and all of the measurements to be coherently combined. The distributed case offers the additional flexibility of deploying the radar modules widely separated with arbitrary standoff distances either along the front wall or surrounding the scene of interest. As such, the aspect and/or bistatic angles and, in turn, the RCS changes across the units. Therefore, the acquired measurements cannot be combined coherently.

In the sequel, the signal models for the two cases are developed. We consider measurement vectors $\{\bar{\boldsymbol{z}}_{s^{\mathrm{Tx}}s^{\mathrm{Rx}}}; s^{\mathrm{Tx}}, s^{\mathrm{Rx}} = 0, \ldots, S-1\}$, where s^{Tx} and s^{Rx} are the indices of the transmitting and receiving modules, respectively. Likewise, the dictionaries $\tilde{\boldsymbol{\Psi}}_{s^{\mathrm{Tx}}s^{\mathrm{Rx}}}(\boldsymbol{w})$ are indexed by the transmitting and receiving modules, whereas the wall position vector $\boldsymbol{w}$ is universal. Finally, the spatial downsampling operation for the transmitting module s^{Tx} is denoted as $\boldsymbol{\Phi}_s^{\mathrm{Tx}}$, while $\boldsymbol{\Phi}_s^{\mathrm{Rx}}$ represents the downsampling matrix for the receiving module s^{Rx}, which includes not only the spatial downsampling of the N receivers but also the linear mixing scheme for downsampling in the time domain. An additive noise vector $\boldsymbol{n}$ for the full received signal is also considered. Using the above notation, the signal model in the co-located case can be expressed as

$$\begin{bmatrix} \bar{\boldsymbol{z}}_{0\ 0} \\ \bar{\boldsymbol{z}}_{0\ 1} \\ \vdots \\ \bar{\boldsymbol{z}}_{0\ S-1} \\ \vdots \\ \bar{\boldsymbol{z}}_{S-1\ S-1} \end{bmatrix} = \begin{pmatrix} \boldsymbol{\Phi}_0^{\mathrm{Tx}}\boldsymbol{\Phi}_0^{\mathrm{Rx}}\tilde{\boldsymbol{\Psi}}_{0\ 0}(\boldsymbol{w}) \\ \boldsymbol{\Phi}_0^{\mathrm{Tx}}\boldsymbol{\Phi}_1^{\mathrm{Rx}}\tilde{\boldsymbol{\Psi}}_{0\ 1}(\boldsymbol{w}) \\ \vdots \\ \boldsymbol{\Phi}_0^{\mathrm{Tx}}\boldsymbol{\Phi}_{S-1}^{\mathrm{Rx}}\tilde{\boldsymbol{\Psi}}_{0\ S-1}(\boldsymbol{w}) \\ \vdots \\ \boldsymbol{\Phi}_{S-1}^{\mathrm{Tx}}\boldsymbol{\Phi}_{S-1}^{\mathrm{Rx}}\tilde{\boldsymbol{\Psi}}_{S-1\ S-1}(\boldsymbol{w}) \end{pmatrix} \tilde{\boldsymbol{\sigma}} + \boldsymbol{n}. \tag{6}$$

Note that a common reflectivity vector $\tilde{\boldsymbol{\sigma}}$ is sufficient for all combinations of the various modules, as the target RCS is assumed to be the same in this case.

In contrast to the co-located configuration, a separate reflectivity vector $\tilde{\boldsymbol{\sigma}}_{s^{\mathrm{Tx}}s^{\mathrm{Rx}}}$ for each combination of s^{Tx} and s^{Rx} has to be introduced in the distributed case. This accounts for the RCS change that is inherent in a distributed aperture scenario. Hence, we obtain the signal

model

$$\begin{bmatrix} \bar{\boldsymbol{z}}_{0\ 0} \\ \bar{\boldsymbol{z}}_{0\ 1} \\ \vdots \\ \bar{\boldsymbol{z}}_{0\ S-1} \\ \vdots \\ \bar{\boldsymbol{z}}_{S-1\ S-1} \end{bmatrix} = \mathrm{bd}\begin{pmatrix} \boldsymbol{\Phi}_0^{\mathrm{Tx}}\boldsymbol{\Phi}_0^{\mathrm{Rx}}\tilde{\boldsymbol{\Psi}}_{0\ 0}(\boldsymbol{w}) \\ \boldsymbol{\Phi}_0^{\mathrm{Tx}}\boldsymbol{\Phi}_1^{\mathrm{Rx}}\tilde{\boldsymbol{\Psi}}_{0\ 1}(\boldsymbol{w}) \\ \vdots \\ \boldsymbol{\Phi}_0^{\mathrm{Tx}}\boldsymbol{\Phi}_{S-1}^{\mathrm{Rx}}\tilde{\boldsymbol{\Psi}}_{0\ S-1}(\boldsymbol{w}) \\ \vdots \\ \boldsymbol{\Phi}_{S-1}^{\mathrm{Tx}}\boldsymbol{\Phi}_{S-1}^{\mathrm{Rx}}\tilde{\boldsymbol{\Psi}}_{S-1\ S-1}(\boldsymbol{w}) \end{pmatrix} \begin{bmatrix} \tilde{\boldsymbol{\sigma}}_{0\ 0} \\ \tilde{\boldsymbol{\sigma}}_{0\ 1} \\ \vdots \\ \tilde{\boldsymbol{\sigma}}_{0\ S-1} \\ \vdots \\ \tilde{\boldsymbol{\sigma}}_{S-1\ S-1} \end{bmatrix} + \boldsymbol{n}, \tag{7}$$

where $\mathrm{bd}(\cdot)$ denotes the block diagonal matrix operation. Note that the number of unknowns has increased S^2-fold as compared to the co-located case. However, this increase can be compensated by exploiting the structure contained in the combined vector of unknowns. Essentially, each transmit-receive module pair observes the same scene of interest, potentially from a different vantage point. As the positions of the radar modules are assumed to be known, the image grid can be chosen, such that the individual sub-images are represented in the same global coordinate system. Hence, the locations of the targets in this global coordinate system are invariant. This results in a group sparse structure, and all $\tilde{\boldsymbol{\sigma}}_{s^{\mathrm{Tx}}s^{\mathrm{Rx}}}$ vectors share a common support or sparsity pattern which will be detailed in a later section.

C. Analytical Comparison of the Dictionaries

In order to compare the co-located and distributed cases, we analyze the two dictionaries in the respective models (6) and (7) in more detail. In both cases, the dictionary matrices are composed of the same blocks $\boldsymbol{\Phi}_{s^{\mathrm{Tx}}}^{\mathrm{Tx}}\boldsymbol{\Phi}_{s^{\mathrm{Rx}}}^{\mathrm{Rx}}\tilde{\boldsymbol{\Psi}}_{s^{\mathrm{Tx}}s^{\mathrm{Rx}}}$, $\quad s^{\mathrm{Tx}}, s^{\mathrm{Rx}} = 0, \ldots, S-1$. For notational convenience, a linear index for the S^2 blocks is used, i.e., $q = 0, \ldots, Q-1, Q = S^2$, and the dictionary blocks are represented by

$$\boldsymbol{A}^{(q)} = \boldsymbol{\Phi}_{s^{\mathrm{Tx}}}^{\mathrm{Tx}}\boldsymbol{\Phi}_{s^{\mathrm{Rx}}}^{\mathrm{Rx}}\tilde{\boldsymbol{\Psi}}_{s^{\mathrm{Tx}}s^{\mathrm{Rx}}}, \quad s^{\mathrm{Tx}} = \left\lfloor \frac{q}{S} \right\rfloor,$$
$$s^{\mathrm{Rx}} = q \mod S, \quad q = 0, \ldots, Q-1.$$

Hence, the dictionary in the co-located model (6) can be expressed as

$$\boldsymbol{A}_{\text{co-loc}} = \left[\left(\boldsymbol{A}^{(0)}\right)^T, \ldots, \left(\boldsymbol{A}^{(Q-1)}\right)^T \right]^T \tag{8}$$

and the one for the distributed model (7) as

$$\boldsymbol{A}_{\text{distr}} = \mathrm{bd}(\boldsymbol{A}^{(0)}, \ldots, \boldsymbol{A}^{(Q-1)}). \tag{9}$$

First, we compare the two dictionaries in terms of their coherence. For a dictionary $\boldsymbol{A}$, the coherence is defined as [30]

$$\mu(\boldsymbol{A}) = \max_{k,l\neq k} \frac{|\boldsymbol{a}_k^H \boldsymbol{a}_l|}{\|\boldsymbol{a}_k\|_2 \|\boldsymbol{a}_l\|_2}, \tag{10}$$

where $\boldsymbol{a}_k$ denotes the k-th column of $\boldsymbol{A}$ and $(\cdot)^H$ denotes the Hermitian transpose. In other words, the coherence of a dictionary can be seen as the maximum correlation between any two of its columns. Without loss of generality, we assume that the columns of the sub-matrices $\boldsymbol{A}^{(q)}$ in (8) and (9) are normalized, i.e. $\|\boldsymbol{a}_k^{(q)}\|_2 = 1, \forall q = 0, \ldots, Q-1, k = 0, \ldots, P-1$. Further, we define the coherence values of the sub-matrices as $\mu(\boldsymbol{A}^{(q)}) = \mu_q, q = 0, \ldots, Q-1$. For the co-located case, the coherence is given by

$$\begin{aligned}
&\mu(\boldsymbol{A}_{\text{co-loc}}) \\
&= \max_{k,l\neq k} \frac{\left| \left(\boldsymbol{a}_k^{(0)}\right)^H \boldsymbol{a}_l^{(0)} + \cdots + \left(\boldsymbol{a}_k^{(Q-1)}\right)^H \boldsymbol{a}_l^{(Q-1)} \right|}{\left\| \left(\boldsymbol{a}_k^{(0)}\right)^T, \ldots, \left(\boldsymbol{a}_k^{(Q-1)}\right)^T \right\|_2 \left\| \left(\boldsymbol{a}_l^{(0)}\right)^T, \ldots, \left(\boldsymbol{a}_l^{(Q-1)}\right)^T \right\|_2} \\
&\leq \frac{\max\limits_{k,l\neq k} \left| \left(\boldsymbol{a}_k^{(0)}\right)^H \boldsymbol{a}_l^{(0)} \right| + \cdots + \max\limits_{k,l\neq k} \left| \left(\boldsymbol{a}_k^{(Q-1)}\right)^H \boldsymbol{a}_l^{(Q-1)} \right|}{\sqrt{Q}\sqrt{Q}} \\
&= \frac{1}{Q} \sum_{q=0}^{Q-1} \mu_q.
\end{aligned} \tag{11}$$

In essence, the overall dictionary coherence is the average of the individual coherences of the sub-matrices.

For the distributed case, we obtain

$$\mu(\boldsymbol{A}_{\text{distr}}) = \max_q \max_{k,l\neq k} \frac{\left| \left(\boldsymbol{a}_k^{(q)}\right)^H \boldsymbol{a}_l^{(q)} \right|}{\left\| \left(\boldsymbol{a}_k^{(q)}\right) \right\|_2 \left\| \left(\boldsymbol{a}_l^{(q)}\right) \right\|_2} = \max_q \mu_q, \tag{12}$$

which implies that the overall dictionary coherence is the maximum of the individual coherences of the sub-matrices. Clearly, $\mu(\boldsymbol{A}_{\text{distr}}) \geq \mu(\boldsymbol{A}_{\text{co-loc}})$. Furthermore, the distributed configuration suffers from the Q-fold increase in the ambient dimension and in the number of non-zero elements in the solution which puts it at a disadvantage compared to the co-located case. However, there is an important underlying structure of the solution of equation (7) which should be recognized. Since all sub-vectors $\tilde{\boldsymbol{\sigma}}_{s^{\text{Tx}}s^{\text{Rx}}}$ in (7) share the same sparsity pattern, rather than calculating the coherence of $\boldsymbol{A}_{\text{distr}}$, we should determine the block-coherence of the dictionary as proposed in [31]. In so doing, we capture the advantage of exploiting the block-structure of the solution.

The block-coherence of a dictionary $\boldsymbol{A}$ is defined as [31]

$$\mu_{\mathrm{B}}(\boldsymbol{A}) = \max_{k,l\neq k} \frac{1}{d}\rho(\boldsymbol{A}_k^H \boldsymbol{A}_l), \tag{13}$$

where d denotes the block size, $\rho(\cdot)$ is the spectral norm, i.e. the maximum eigenvalue of the matrix argument, and $\boldsymbol{A}_l$ is the sub-matrix of $\boldsymbol{A}$ that contains all columns belonging to the l-th block. The definition of block-coherence (13) assumes that the group sparse dictionary atoms reside in adjacent columns. However, for the problem at hand, a group consists of all columns associated with a certain target for any radar unit pair. As these columns are not adjacent to each other in $\boldsymbol{A}_{\text{distr}}$, the dictionary needs to be rearranged. The permuted dictionary is defined as

$$\tilde{\boldsymbol{A}}_{\text{distr}} = [\mathrm{blkdiag}(\boldsymbol{a}_0^{(0)}, \ldots, \boldsymbol{a}_0^{(Q-1)}), \ldots, \mathrm{blkdiag}(\boldsymbol{a}_{P-1}^{(0)}, \ldots, \boldsymbol{a}_{P-1}^{(Q-1)})], \tag{14}$$

which obeys the block-structure as assumed in (13). This yields the block-coherence in the distributed configuration as

$$\begin{aligned}
&\mu_{\mathrm{B}}(\tilde{\boldsymbol{A}}_{\text{distr}}) \\
&= \max_{k,l\neq k} \frac{1}{Q}\rho\left(\mathrm{bd}(\boldsymbol{a}_k^{(0)}, \ldots, \boldsymbol{a}_k^{(Q-1)})^H \mathrm{bd}(\boldsymbol{a}_l^{(0)}, \ldots, \boldsymbol{a}_l^{(Q-1)})\right) \\
&= \max_{k,l\neq k} \frac{1}{Q}\rho\left(\mathrm{diag}\left(\left(\boldsymbol{a}_k^{(0)}\right)^H \boldsymbol{a}_l^{(0)}, \ldots, \left(\boldsymbol{a}_k^{(Q-1)}\right)^H \boldsymbol{a}_l^{(Q-1)}\right)\right) \\
&= \max_{k,l\neq k} \frac{1}{Q} \max_q \left(\left|\left(\boldsymbol{a}_k^{(0)}\right)^H \boldsymbol{a}_l^{(0)}\right|, \ldots, \left|\left(\boldsymbol{a}_k^{(Q-1)}\right)^H \boldsymbol{a}_l^{(Q-1)}\right|\right) \\
&= \frac{1}{Q}\max_q \mu_q = \frac{1}{Q}\mu(\boldsymbol{A}_{\text{distr}}),
\end{aligned} \tag{15}$$

which is an improvement by a factor of Q as compared to the conventional coherence.

Finally, a remark on the relation between the dictionary coherence and radar parameters, such as transmit pulse, array geometry or scene discretization, is in order. It has been shown that the dictionary coherence is closely related to the radar ambiguity function (AF) [32]. In the far-field, the AF can be easily calculated and the values only depend on the transmit pulse, delay, and Doppler. However, in the near-field and bistatic radar case, the AF always depends on the radar geometry. For the considered multipath exploitation scenario, the room geometry also needs to be taken into account, as multipath affects the coherence of the dictionary. These factors render the derivation of the analytic expressions or bounds for the coherence values quite challenging.

Instead, we compute the coherence and provide the corresponding values for the simulation examples in Section IV.

Having derived the coherence values in (11), (12) and (15), we next compare the reconstruction guarantees for the corresponding cases. For the noise-free signal model, an upper limit on the sparsity for successful scene reconstruction is given as [30], [33]

$$K < \frac{1}{2}(\mu^{-1} + 1), \tag{16}$$

where K is the sparsity level of the scene. A similar condition for block sparse reconstruction can be expressed as [31]

$$K < \frac{1}{2d}(\mu_{\mathrm{B}}^{-1} + d). \tag{17}$$

For the considered configurations, we obtain the following upper bounds on the number of targets (or sparsity of the scene) for successful scene recovery,

$$K_{\text{co-loc}} < \frac{1}{2}(\mu(\boldsymbol{A}_{\text{co-loc}})^{-1} + 1) \tag{18}$$

$$K_{\text{distr,nonblk}} < \frac{1}{2Q}(\mu(\boldsymbol{A}_{\text{distr}})^{-1} + 1) \tag{19}$$

$$K_{\text{distr,blk}} < \frac{1}{2Q}(\mu_{\mathrm{B}}(\tilde{\boldsymbol{A}}_{\text{distr}})^{-1} + Q) = \frac{1}{2}(\mu(\boldsymbol{A}_{\text{distr}})^{-1} + 1). \tag{20}$$

It is clear that without considering the block structure for the distributed case, the maximum number of targets is reduced by approximately a factor of Q from the co-located to the distributed configuration. However, when exploiting the group structure, the maximum number of targets $K_{\text{distr,blk}}$ is of the same order as for the co-located case. Further, note that equations (18)-(20) do not hold exactly in the presence of noise. However, they are expected to give a reasonable indication of the reconstruction performance. This will be supported by simulation in Section IV.

III. Sparse Scene Reconstruction under Known and Uncertain Wall Positions

In this section, we first briefly review the sparsity based approach for scene reconstruction with a single radar module under known wall locations. Next, we present the method to deal with multiple radar modules for known wall locations. Subsequently, we propose the sparse reconstruction method under wall location uncertainties.

A. Single Module and Known Wall Locations

Given the measurements $\bar{\boldsymbol{z}}$ of a single unit in (5), we aim at recovering the scene $\tilde{\boldsymbol{\sigma}}$ using sparse reconstruction. As the same physical scene is observed via all R paths, the vectorized scene $\tilde{\boldsymbol{\sigma}}$ exhibits a group sparse structure, with the group extending across the R paths for each target location [16]. Employing a group sparse reconstruction approach results in a mixed ℓ_1-ℓ_2 norm optimization problem [14], [16]

$$\hat{\tilde{\boldsymbol{\sigma}}} = \arg\min_{\tilde{\boldsymbol{\sigma}}} \|\bar{\boldsymbol{z}} - \boldsymbol{\Phi}\tilde{\boldsymbol{\Psi}}(\boldsymbol{w})\tilde{\boldsymbol{\sigma}}\|_2^2 + \lambda\|\tilde{\boldsymbol{\sigma}}\|_{1,2}, \tag{21}$$

where

$$\|\tilde{\boldsymbol{\sigma}}\|_{1,2} = \sum_{p=0}^{P-1} \left\| \left[\sigma_p^{(0)}, \sigma_p^{(1)}, \ldots, \sigma_p^{(R-1)}\right]^T \right\|_2, \tag{22}$$

and λ is a regularization parameter. The optimization problem in (21) can be solved using SparSA [34] or other available schemes [31], [35]. Once a solution $\hat{\tilde{\boldsymbol{\sigma}}}$ is obtained, the individual sub-images can be combined noncoherently to form a composite image of the scene of interest. Note that perfect knowledge of $\boldsymbol{w}$ is assumed in this case.

B. Multiple Modules and Known Walls

In the case of multiple modules, we first express the signal models (6) and (7), corresponding to the co-located and distributed configurations, under a common structure as

$$\breve{\boldsymbol{z}} = \breve{\boldsymbol{A}}(\boldsymbol{w})\breve{\boldsymbol{\sigma}} + \boldsymbol{n}. \tag{23}$$

The differences lie in the dimensions of the reflectivity vector $\breve{\boldsymbol{\sigma}}$ and the dictionary $\breve{\boldsymbol{A}}(\boldsymbol{w})$ and the size of the groups in the group sparse reconstruction. A comparison of the relevant properties is provided in Table I. As the measurements from the various modules are coherently combined in the co-located case, the number of unknowns and the group size does not change as compared to the single module case. In fact, the multi-module system is equivalent to a single radar unit with larger arrays. On the other hand, the noncoherent combining of the various measurements in the distributed case cause both the number of unknowns and the group size to increase by a factor of S^2. As discussed in the dictionary analysis, the larger group size at least partly offsets the increase in the number of unknowns.

TABLE I

KEY PARAMETERS IN GROUP SPARSE RECONSTRUCTION

	Single Module	Co-Located	Distributed
No. of transmit-receive module pairs	1	S^2	S^2
No. of unknown reflectivity vectors or sub-images	1	1	S^2
Group size	R	R	RS^2

For the multiple module case, we can employ the same mixed-norm reconstruction as in (21), resulting in

$$\hat{\breve{\boldsymbol{\sigma}}} = \arg\min_{\breve{\boldsymbol{\sigma}}} \|\breve{\boldsymbol{z}} - \breve{\boldsymbol{A}}(\boldsymbol{w})\breve{\boldsymbol{\sigma}}\|_2^2 + \lambda\|\breve{\boldsymbol{\sigma}}\|_{1,2}. \tag{24}$$

Note that the regularization term $\|\breve{\boldsymbol{\sigma}}\|_{1,2}$ depends on the number and structure of the groups. Hence, it differs for the distributed and the co-located cases.

C. Unknown Wall Locations

In practice, precise prior knowledge of the interior wall locations $\boldsymbol{w}$ is usually not available. The walls locations rather have to be estimated from the returns using building layout estimation techniques, such as [36], [2, Ch. 2, p. 49]. These estimates are subject to errors that can be on the order of TWRI system wavelengths. Multipath exploitation requires accurate knowledge of the room layout in order to deliver high quality images. In the presence of wall location errors, two mechanisms lead to degradation of the reconstructed image quality. First, the returns from a specific multipath are coherently combined in the measurement model. Since the wall location errors cause the expected multipath delays to deviate from the actual delays, the coherence of the multipath returns is lost, resulting in a mismatch between the dictionary $\breve{\boldsymbol{A}}(\boldsymbol{w})$ and the received signal. Second, wall location errors may lead to a misalignment of the various sub-images in the signal model, thereby violating the group sparse structure of $\breve{\boldsymbol{\sigma}}$. The perfect alignment of the sub-images is only guaranteed if the multipath delays are equal to the assumed ones.

In order to deal with the aforementioned issues, it is imperative to take wall position uncertainties into account in the reconstruction process. To this end, we propose a joint optimization approach for image reconstruction and wall position estimation, i.e., a joint minimization over

the reflectvity vector $\breve{\boldsymbol{\sigma}}$ and the wall position vector $\boldsymbol{w}$,

$$\min_{\boldsymbol{w},\breve{\boldsymbol{\sigma}}} \|\breve{\boldsymbol{z}} - \breve{\boldsymbol{A}}(\boldsymbol{w})\breve{\boldsymbol{\sigma}}\|_2^2 + \lambda\|\breve{\boldsymbol{\sigma}}\|_{1,2}. \tag{25}$$

Note that the reconstruction problem (25) is now a non-convex optimization problem as the dictionary has a nonlinear dependence on the wall locations. In fact, in the near-field imaging case, there is not even a closed-form solution for the delays contained in the matrix [37], which renders the problem very difficult to solve directly. However, it is always possible to express (25) as a nested optimization problem [38, Ch. 4, p. 133]. Choosing to optimize over $\breve{\boldsymbol{\sigma}}$ first and then over $\boldsymbol{w}$, (25) can equivalently be posed as [27]

$$\min_{\boldsymbol{w}} \min_{\breve{\boldsymbol{\sigma}}} \|\breve{\boldsymbol{z}} - \breve{\boldsymbol{A}}(\boldsymbol{w})\breve{\boldsymbol{\sigma}}\|_2^2 + \lambda\|\breve{\boldsymbol{\sigma}}\|_{1,2}. \tag{26}$$

The overall optimization problem is still non-convex, but it now consists of a convex part and a non-convex part. More specifically, the inner optimization over $\breve{\boldsymbol{\sigma}}$ is convex, which is exactly the same as the reconstruction problem (24) and can be solved efficiently. The outer minimization is non-convex; however, the dimension of the solution space is much smaller and, thus, easier to search. In a typical room, the number of unknown interior wall locations is at the most three, whereas the number of grid points is several orders of magnitude larger. Note that (26) can be seen as a highly-parametrized dictionary learning problem. The parameters $\boldsymbol{w}$ should be learned, such that the sparsest representation of the observed scene is achieved. The high degree of parametrization comes from the physical aspects of wave propagation in the indoor environment, thereby restricting the number of degrees of freedom. Further, although the nested optimization problem is posed for the multiple module case, it is still applicable to the single module based reconstruction under wall location uncertainties as well. This is because the single unit module is a special case of the co-located multiple module configuration with $S = 1$.

The outer nonconvex problem in (26) can be solved by general nonlinear optimization methods. Since there is no closed-form method to compute the dictionary, it is not feasible to find an analytic solution for the gradient of the problem. As such, possible candidates are, among others, Quasi-Newton (QN) methods using finite-difference gradients [39] or heuristic methods, such as particle swarm optimization (PSO) [40], [41]. The benefit of the the Quasi-Newton method is its guaranteed convergence. However, the solutions of the inner convex optimization problem must be very accurate in order to prevent erroneous finite-difference estimates of the

gradient for QN methods. Provided that the estimates of the gradient are sufficiently accurate, the objective value decreases at every iteration. As the objective function in (26) is bounded below, the algorithm will always converge to a local minimum. Since the objective function is non-convex and, therefore, may have many local minima, finding a local minimum is not equivalent to finding the global minimum. In general, we cannot make any claims about the "goodness" of the local minimum found. On the other hand, being a heuristic method, PSO has no performance guarantees. However, it does provide a certain probability of overcoming local minima and descending closer to the global minimum. We support these considerations with numerical results using simulated and measured data in Section IV.

A remark on the computational complexity of the proposed reconstruction approach is in order. The computational complexity lies mainly in calculation of the propagation delays for the dictionaries and in evaluating the matrix-vector multiplications in equations (6) and (7) or their adjoint versions. In order to solve one instance of (24), the delays should be calculated once, whereas the matrix-vector multiplications are carried out multiple times due to the iterative nature of the available solvers. For simplicity, we compare the QN method with PSO by counting the number of mixed-norm problems (24) that need to be solved. Based on extensive simulations, we found that PSO usually required roughly ten times the number of solved sub-problems as compared to QN method. The detailed results are provided in Section IV. In general, the wall error correction method results in much higher numerical cost as compared to the known wall location case.

IV. Simulation and Experimental Results

A. Simulation Results

Simulations were performed for a simple rectangular room enclosed by four homogeneous walls. The size of the room is 4 m by 4 m, i.e., the walls are located 2 m away in crossrange from the center of the room. The walls are modeled with thickness $d = 20$ cm and relative permittivity $\epsilon_r = 7.66$, which is typical of concrete. We consider$S = 2$ radar modules, each being a wideband real aperture pulsed radar with a uniform linear array of $N = 3$ receivers and an inter-element spacing of 10 cm. The central element of each receive array also acts as a transmitter, i.e., $M = 1$. We examine three different scenarios to compare co-located and distributed placements of the modules. Access to the outside perimeter of the room from up to

two different sides is assumed. When one module is transmitting, both modules simultaneously record the returns with their respective receive arrays. All measurements are finally assumed to be available at a single data processing center where the scene reconstruction is carried out.

Each module is oriented parallel to the wall facing it and is positioned at a stand-off distance of 3 m from the wall. Each radar module transmits modulated Gaussian pulses, centered at $f_c = 2$ GHz, with a relative bandwidth of 50%. At each element of the receive arrays, $T = 150$ fast time samples are collected in the relevant interval, covering the target and multipath returns with a sampling rate of $f_s = 4$ GHz. For each array, each side wall is assumed to cause 3 different multipath returns; multipath associated with the back wall is not considered. For each side wall, we observe two different first-order multipath returns. A first-order multipath involves only one secondary reflection at an interior wall, which could take place either on the way from the transmitter to the target or from the target back to the receiver. Also, we consider one second-order multipath for each side wall, where a secondary reflection takes place at the same interior wall on both legs of the round-trip path. In total, there are $R = 7$ paths that are considered in the received signal corresponding to each transmit-receive pair. The multipath returns are all considered to be 6 dB weaker than the direct path. Further, we assume that the returns from the front wall have been properly suppressed. In all the simulations, complex circular Gaussian noise with 20 dB signal-to-noise ratio (SNR) is added to the simulated measurements. Further, as we are focusing on the benefit of sparse reconstruction rather than reduction in the number of measurements, we do not employ any downsampling operation in the simulations.

The imaged region extends 5 m each in crossrange and downrange and is centered at (0 m,5 m), which is the center of the room.The scene is spatially discretized into $P = 64 \times 64$ pixels. Errors in positions of the front and back walls are not considered, since the multipath returns are assumed to be due to secondary reflections at the side walls only. The initial estimate of the locations of the side walls is drawn from a uniform distribution. The distribution is centered around the true wall locations and extends to errors of ± 0.5 m. In essence, we are assuming that a building layout estimation technique has been applied to the data beforehand yielding the estimates of the side wall locations, which are within a 0.5 m error margin. The specific error margin is chosen in accordance with the specifications of the VisiBuilding Program by the U.S. Defense Advanced Research Projects Agency [42]. As such, the search space of the proposed dictionary learning method is limited by box constraints centered around the initial

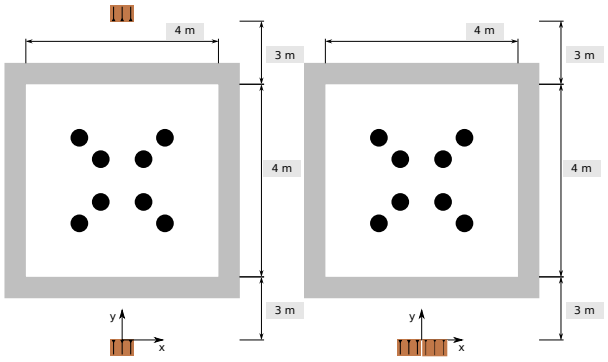

(a) Distributed units (b) Co-located units

Fig. 1. Scene geometries for Scenario A.

estimates of the wall locations. We use the Matlab implementation of a Quasi- Newton method and a particle swarm optimization toolbox for Matlab [43] for solving the outer non-convex optimization problem in the simulations, whereas SparSA [34] is used to solve the inner convex problem. Note that the optimal choice of the regularization parameter λ is still an open problem and has not been considered in this work. A common heuristic $\lambda = \lambda_{\text{norm}} \|\breve{\boldsymbol{A}}(\boldsymbol{w})^H \breve{\boldsymbol{z}}\|_\infty$ has been used, with $\lambda_{\text{norm}} = 0.3$. The specific scene layout in terms of the TWRI module placements and the number and locations of the targets in the room are described below for each of the considered scenarios separately.

1) Scenario A: In Scenario A, eight point targets of equal reflectivity are considered at specific locations in the room, as illustrated in Fig. 1. We consider both co-located and distributed configurations. For the distributed configuration, the two modules are located on opposing sides of the room, as shown in Fig. 1a, whereas both modules are placed next to each other facing the front wall in the co-located case. Example reconstructions of the scene under various conditions are depicted in Fig.2. We observe that the scene is reconstructed almost perfectly for both configurations, if prior knowledge of the exact wall locations is available, refer to Figs. 2a,d. However, if the initial estimates of the side wall positions are set to 1.6 m and -1.7 m with respect to the y-axis of the coordinate system, image reconstruction fails completely for both distributed and co-located configurations, see Figs. 2b,e. This validates the need for the proposed wall correction method, whose applications to the considered scene and radar configurations yield the images in Figs. 2c,f. Evidently, the PSO approach is able to enhance the image quality, with

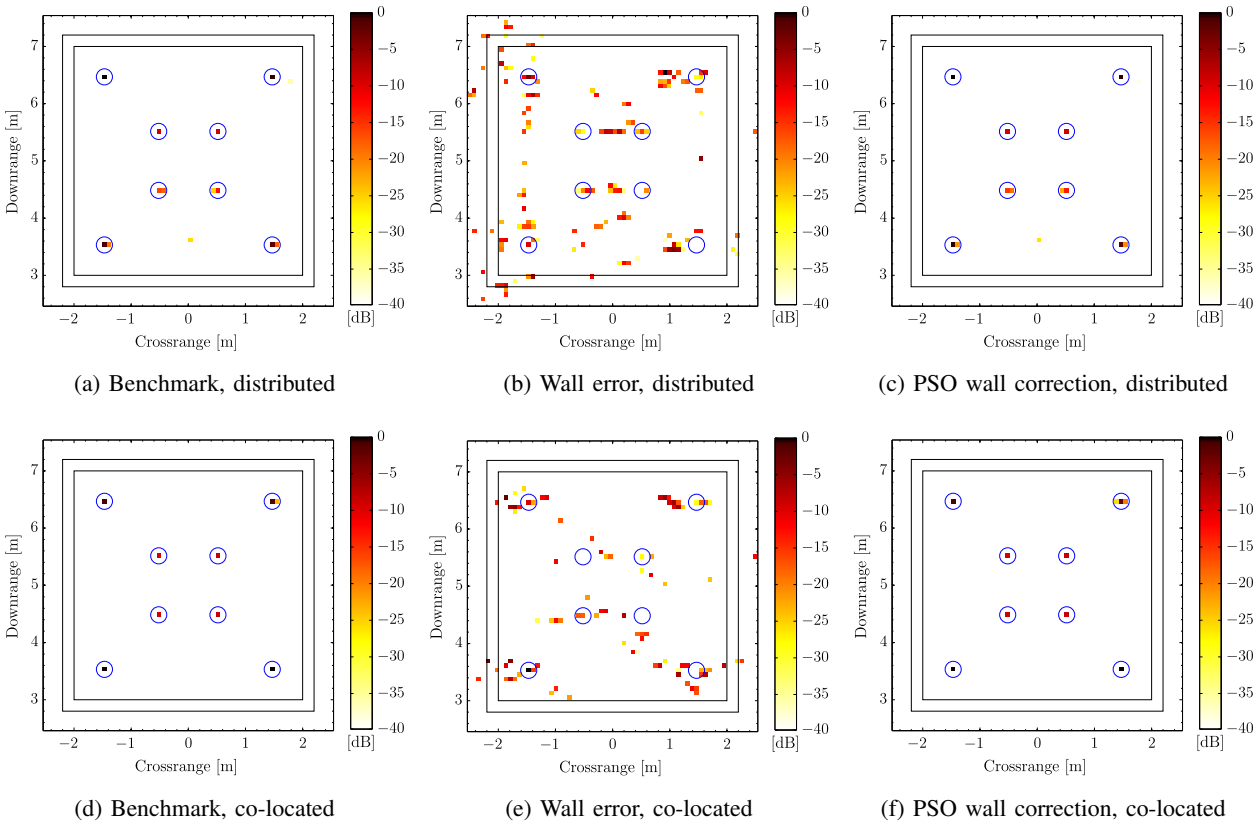

(a) Benchmark, distributed (b) Wall error, distributed (c) PSO wall correction, distributed

(d) Benchmark, co-located (e) Wall error, co-located (f) PSO wall correction, co-located

Fig. 2. Reconstruction results for Scenario A: Opposing walls versus same wall placement.

the result being on par with the known wall location or benchmark case. The estimated wall positions are 1.999 m and -2.003 m for the distributed case and 1.999 m and -2.001 m for the co-located case. Hence, the estimation error is in the millimeter range for both configurations.

The coherence of the dictionary has been computed for both the co-located and the distributed configurations, refer to Table II. The individual coherence values are listed for each module pair, i.e. the indices of the transmitting and receiving module. Observe that the distributing the radar modules has a slight advantage as reflected in the lower row of Table II. Using (11) and (15), the coherence for the overall radar imaging system can also be calculated. For the co-located case, we obtain $\mu(\boldsymbol{A}_{\text{co-loc}}) = 0.1415$, whereas the distributed case yields $\mu_{\text{B}}(\tilde{\boldsymbol{A}}_{\text{distr}}) = 0.1413$. Hence, the final coherence values are approximately equal. This is because the coherence in the distributed configuration is dominated by the least favorable module pair, which in turn corresponds to a co-located array.

In order to obtain a quantitative measure for the reconstruction performance, a full reference

TABLE II

SCENARIO A: COHERENCE VALUES FOR MODULE PAIRS

Modules	0;0	0;1	1;0	1;1
co-loc	0.5670	0.5662	0.5662	0.5654
dist	0.5654	0.4272	0.4272	0.5654

image quality metric is used. We compare the ideal image, i.e., the ground truth, with the reconstructions using the Earth Mover's Distance (EMD), which computes the amount of "dirt" or image intensity that has to be moved to get from one image to the other [44]. We normalize all images to have a maximum intensity of one; further, the pixel distance is also normalized to one and thresholded at five. That is, if the strongest pixel is off by one, the resulting EMD is also one. We use a fast EMD implementation by Pele and Werman as proposed in [45]. The mean and standard deviation of the EMD for 50 Monte Carlo runs are listed in Table III for the various considered cases. Apparently, the distributed setup fails to reconstruct the scene reliably, as the error and the variance are relatively large not only for the wall location correction methods but also the benchmark case. In the co-located case, the wall correction methods almost achieve the same image quality as the benchmark reconstruction, where the PSO method is outperforming the QN method.

TABLE III

SCENARIO A: EMD COMPARISON ACROSS 50 MONTE CARLO RUNS.

	Wall error		Benchmark		QN corr.		PSO corr.	
	dist	co-loc	dist	co-loc	dist	co-loc	dist	co-loc
mean	161.69	61.54	19.01	3.89	28.50	5.63	56.89	3.94
median	149.33	57.59	6.31	3.83	11.03	3.77	5.48	3.85
std. dev.	88.20	25.26	69.75	0.48	31.44	4.62	337.68	0.50

2) Scenario B: Scenario B compares co-located and distributed placements of two modules along the front wall. The number of targets for this case has been reduced to four. The targets are placed in pairs, with one target directly in front of the other for each pair. However, for now, we do not consider any shadowing, i.e. the wave can travel directly to the rear targets and is not assumed to be blocked by the targets in the front. The scene layout is illustrated in Fig. 3.

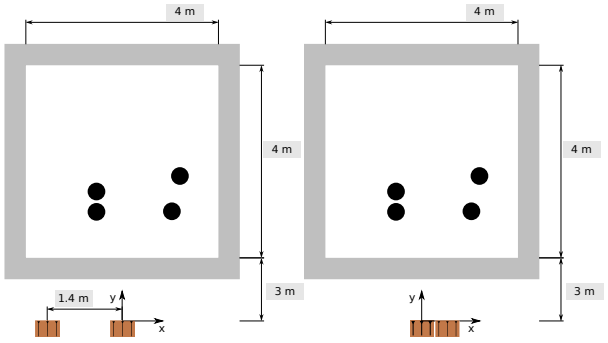

(a) Distributed units (b) Co-located units

Fig. 3. Scene geometries for Scenarios B and C.

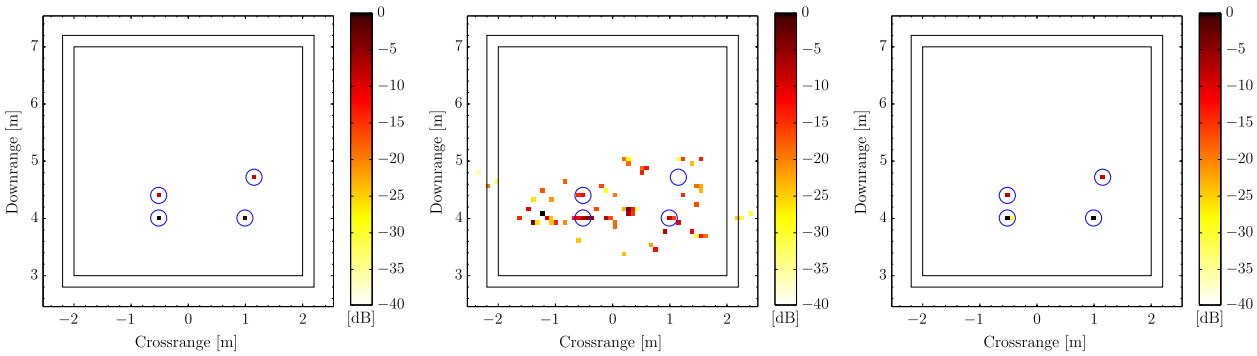

(a) Benchmark, distributed (b) Wall error, distributed (c) PSO wall correction, distributed

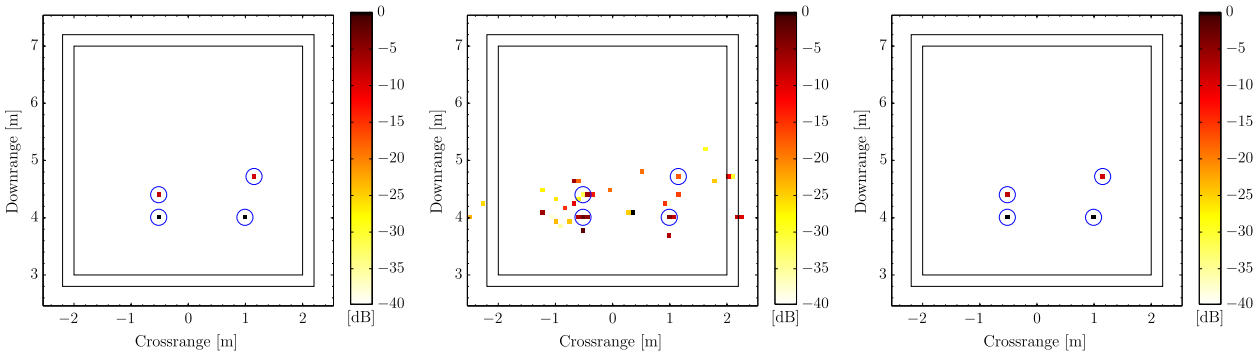

(d) Benchmark, co-located (e) Wall error, co-located (f) PSO wall correction, co-located

Fig. 4. Reconstruction results for Scenario B: Widely-spaced versus closely-spaced placement without shadowing.

Corresponding example reconstructions for the various considered cases are shown in Fig. 4. As expected, the sparse reconstruction fails for erroneous wall locations, whereas the proposed wall location correction scheme based on the PSO method yields almost perfect images of the scene

for both distributed and co-located cases. This performance is also reflected by the high-accuracy of the wall locations estimates; 2.001 m and -1.999 m for the distributed case and 1.998 m and -2.000 m for the co-located case. The above qualitative observations are also confirmed by the quantitative EMD results summarized in Table III. As expected from the theoretical dictionary analysis, the distributed case is slightly inferior to the co-located case. Note that for some noise realizations the reconstruction fails, leading to outliers in the EMD values. Hence, the median may give a better indication of the average or expected performance.

TABLE IV

SCENARIO B: EMD COMPARISON ACROSS 50 MONTE CARLO RUNS.

	Wall error		Benchmark		QN corr.		PSO corr.	
	dist	co-loc	dist	co-loc	dist	co-loc	dist	co-loc
mean	51.98	36.50	1.64	1.39	5.57	1.62	4.98	1.42
median	45.31	36.55	1.59	1.41	1.95	1.42	1.56	1.40
std. dev.	28.71	19.51	0.42	0.24	5.72	0.94	17.45	0.34

3) Scenario C: Scenario C was designed to evaluate the impact of target shadowing on the imaging performance of distributed and co-located configurations. The layout of the scene is exactly the same as in Scenario B; however, we include shadowing of the two rear targets. In particular, the line-of-sight between the two rear targets and the radar module located at zero crossrange (right module in Fig. 3a and the left module in Fig. 3b) is assumed to be blocked. This means that any path involving this line of sight is unavailable, whereas indirect propagation to the centered module is still observable. In total, 11 paths out of 28 (7 paths for 2 by 2 modules) are blocked in this scenario. This introduces two problems in the data measurements. First, the total energy returned from the shadowed targets is lowered leading to a decreased SNR. Second, the structural assumptions on the sparse solutions are violated. Since a number of transmit-receive combinations capture a zero reflectivity, the common support assumption of the reflectivity vectors corresponding to various transmit-receive module pairs is no longer satisfied for the distributed configuration, whereas the assumption of invariant target reflectivity for all combinations of the various modules is no longer valid for the co-located case.

Fig. 5 shows the same selection of example results as in Fig. 4. Comparing Figs. 5a,d and Fig. 4a,d, it is evident that the intensity of the shadowed targets is decreased even for perfectly

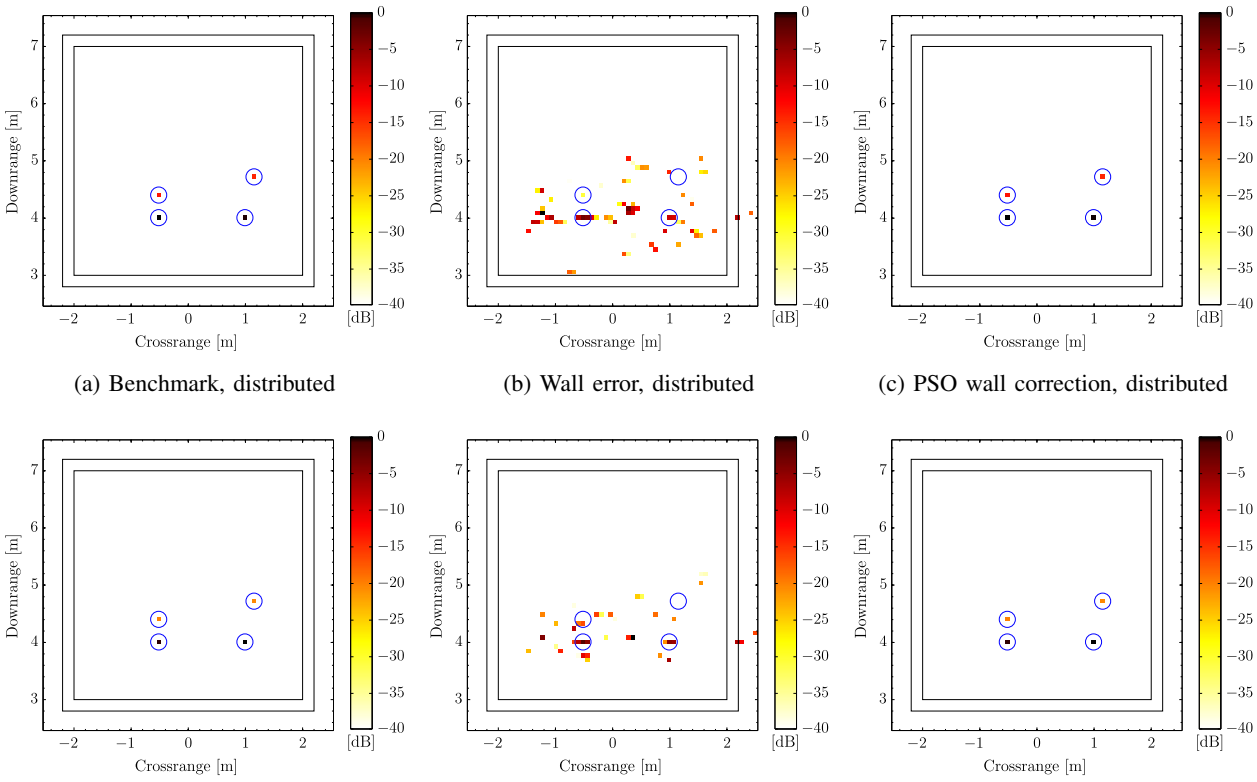

(a) Benchmark, distributed (b) Wall error, distributed (c) PSO wall correction, distributed

(d) Benchmark, co-located (e) Wall error, co-located (f) PSO wall correction, co-located

Fig. 5. Reconstruction results for Scenario C: Widely-spaced versus closely-spaced placement including shadowing.

known side walls. We observe that the co-located configuration shows weak reconstructions for both of the shadowed targets for benchmark as well as wall correction methods, as seen in Figs. 5d,f. On the other hand, the benchmark and wall corrected reconstructions for the distributed case in Fig. 5a,c depict the shadowed targets about 6 dB stronger than in the co-located case. As in the previous examples, the sparse reconstruction without wall error correction, depicted in Figs. 5b,e, fails. Furthermore, accurate wall location estimation results are obtained: 2.000 m and -2.005 m for the distributed and 2.000 m and -1.999 m for the co-located case. It appears that violation of the softer group sparsity constraint is less damaging than the violation of the invariant target reflectivity. As such, despite the theoretical advantages of the co-located configuration under ideal conditions, the distributed configuration stands a better chance of locating targets in shadowing situations.

These observations are confirmed by the EMD based Monte Carlo results, summarized in Table V. For known wall locations and PSO-based wall error correction, median reconstruction

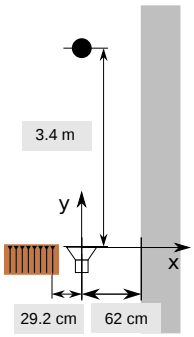

Fig. 6. Scene geometry for the lab experiment.

performance in the distributed case slightly outperforms a co-located placement of the units. The inferior performance of the distributed layout in the mean EMD is attributed to outliers in the reconstruction results. The rather small difference in the EMD between the distributed and co-located cases can be explained by the working principle of the metric. In case of a target intensity mismatch in the reconstructed image, the difference in intensity is penalized. Hence, a difference of 6 dB in the target amplitude does not result in a large difference in the EMD.

TABLE V

SCENARIO C: EMD COMPARISON ACROSS 50 MONTE CARLO RUNS.

	Wall error		Benchmark		QN corr.		PSO corr.	
	dist	co-loc	dist	co-loc	dist	co-loc	dist	co-loc
mean	45.08	35.01	4.16	3.97	7.28	4.07	3.22	3.97
median	41.78	31.83	3.10	3.96	3.34	3.98	3.11	3.98
std. dev.	23.26	21.85	7.15	0.26	9.07	0.59	0.59	0.25

B. Experimental Results

In this section, we present experimental results for a wideband real aperture pulse-Doppler radar with $M = 1$ transmitter and a uniform linear array with $N = 8$ receivers and and inter-element spacing of 6 cm. This is equivalent to a co-located configuration of two modules, each with a single transmitter and a 4-element uniform linear array of receivers, but with only one of the transmitters in operation. The data has been collected in a semi-controlled environment at the Radar Imaging Lab, Villanova University. The transmit waveform is a modulated Gaussian

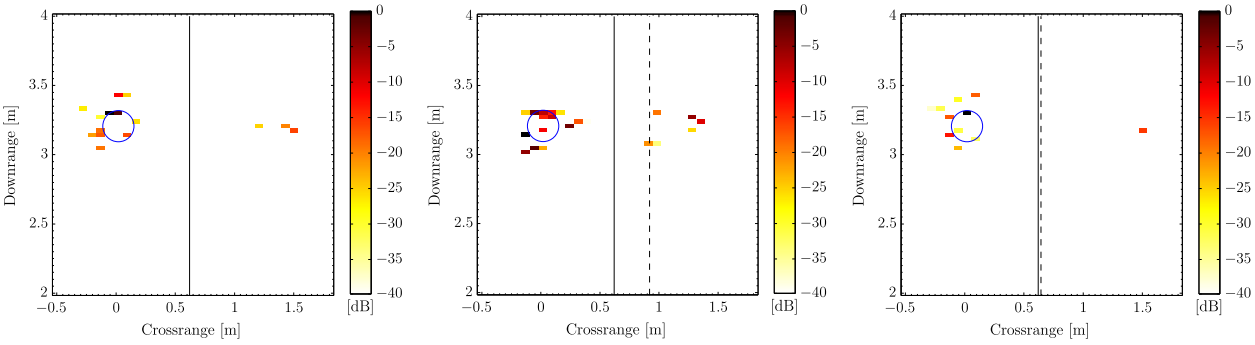

(a) Benchmark (b) Wall error (c) PSO wall correction

Fig. 7. Reconstruction result using experimental data with one unknown side wall.

pulse with center frequency $f_c = 3$ GHz and 100% relative bandwidth. We recorded 768 fast time samples at a sampling rate $f_s = 7.68$ GHz and then gated out the early and late returns to clean the data, resulting in $T = 153$ samples over the interval of interest. The transmitter and the receive array were placed on the same baseline with a lateral spacing of 29.2 cm and the distance of the transmitter to a 0.3 m thick reinforced concrete side wall was 62 cm. The placement of a front wall in the scene was omitted for experimental convenience. If present, the direct scatterings from the wall could be either mitigated [46] or gated out [29]. We consider $R = 4$ propagation paths, i.e. the direct path, two paths with a single reflection at the side wall and one with double reflection at the side wall. The scene consists of a single aluminum pipe placed at 3.4 m downrange directly in front of the transmitter. Refer to Fig. 6 for an illustration of the scene setup.

As a reference, the benchmark result where the actual wall position has been used is shown in Fig. 7a. The reconstruction result with an erroneous wall location is shown in Fig. 7b, whereas the PSO based wall correction result is shown in Fig. 7c. The Quasi-Newton based method yields similar results, omitted here for brevity. The dashed line depicts the assumed and estimated wall locations in Fig. 7b and Fig. 7c, respectively. Similar to the simulation results, we observe that the reconstruction fails when the assumed wall location is incorrect. Using the proposed method, the wall location has been accurately estimated and the corresponding reconstruction yields an image on par with the benchmark.

V. Conclusion

In this paper, we presented a joint sparse image reconstruction and wall location estimation approach for multipath exploitation in TWRI applications. By introducing a parametrized model of the scattering environment, uncertainties in the interior wall locations could be captured and estimated. The resulting optimization problem is convex in the unknown target reflectivities, but non-convex in the wall parameters. An iterative scheme based on a Quasi-Newton method or PSO was proposed to obtain a solution. Although PSO is a purely heuristic method, it showed superior performance in the Monte Carlo simulations. The presented concept could be extended to other parameters, such as wall thickness and permittivity; however, this would require more efficient ways for solving the resulting optimization problem. Furthermore, we proposed and analyzed a flexible modular imaging scheme for TWRI using several man-portable radars, each with limited spatial aperture. The sparse reconstruction approach was extended to deal with both co-located and distributed placements of the modules. Theoretical analysis showed that a co-located placement is generally superior, as it allows for coherent processing of the returns. However, in imaging scenarios where modeling assumptions are violated, a distributed sensor layout may prove to be more robust.

References

[1] M. Amin, Ed., *Through-the-Wall Radar Imaging*. Boca Raton, FL: CRC Press, 2011.

[2] ——, *Compressive Sensing for Urban Radar*. Boca Raton, FL: CRC Press, 2015.

[3] P.-H. Chen, M. Shastry, C.-P. Lai, and R. Narayanan, "A portable real-time digital noise radar system for through-the-wall imaging," *IEEE Transactions on Geoscience and Remote Sensing*, vol. 50, no. 10, pp. 4123–4134, Oct. 2012.

[4] F. Soldovieri, F. Ahmad, and R. Solimene, "Validation of microwave tomographic inverse scattering approach via through-the-wall experiments in semicontrolled conditions," *IEEE Geoscience and Remote Sensing Letters*, vol. 8, no. 1, pp. 123–127, Jan. 2011.

[5] S. Ram, C. Christianson, Y. Kim, and H. Ling, "Simulation and analysis of human micro-dopplers in through-wall environments," *IEEE Transactions on Geoscience and Remote Sensing*, vol. 48, no. 4, pp. 2015–2023, Apr. 2010.

[6] "Special issue on remote sensing of building interior," in *IEEE Transactions on Geoscience and Remote Sensing*, M. G. Amin and K. Sarabandi, Eds., 2009, vol. 47, no. 5, pp. 1270–1420.

[7] M. Dehmollaian and K. Sarabandi, "Refocusing through building walls using synthetic aperture radar," *IEEE Transactions on Geoscience and Remote Sensing*, vol. 46, no. 6, pp. 1589–1599, Jun. 2008.

[8] L.-P. Song, C. Yu, and Q. H. Liu, "Through-wall imaging (TWI) by radar: 2-D tomographic results and analyses," *IEEE Transactions on Geoscience and Remote Sensing*, vol. 43, no. 12, pp. 2793–2798, Dec. 2005.

[9] F. Ahmad, M. G. Amin, and S. A. Kassam, "Synthetic aperture beamformer for imaging through a dielectric wall," *IEEE Transactions on Aerospace and Electronic Systems*, vol. 41, no. 1, pp. 271–283, 2005.

[10] T. Dogaru and C. Le, "SAR images of rooms and buildings based on FDTD computer models," *IEEE Transactions on Geoscience and Remote Sensing*, vol. 47, no. 5, pp. 1388–1401, May 2009.

[11] R. Burkholder, "Electromagnetic models for exploiting multi-path propagation in through-wall radar imaging," in *International Conference on Electromagnetics in Advanced Applications*, Torino, Italy, Sep. 2009, pp. 572–575.

[12] P. Setlur, M. Amin, and F. Ahmad, "Multipath model and exploitation in through-the-wall and urban radar sensing," *IEEE Transactions on Geoscience and Remote Sensing*, vol. 49, no. 10, pp. 4021–4034, Oct. 2011.

[13] G. Gennarelli and F. Soldovieri, "A linear inverse scattering algorithm for radar imaging in multipath environments," *IEEE Geoscience and Remote Sensing Letters*, vol. 10, no. 5, pp. 1085–1089, Sep. 2013.

[14] M. Leigsnering, F. Ahmad, M. Amin, and A. Zoubir, "Multipath exploitation in through-the-wall radar imaging using sparse reconstruction," *IEEE Transactions on Aerospace and Electronic Systems*, vol. 50, no. 2, pp. 920–939, Apr. 2014.

[15] S. Kidera, T. Sakamoto, and T. Sato, "Extended imaging algorithm based on aperture synthesis with double-scattered waves for UWB radars," *IEEE Transactions on Geoscience and Remote Sensing*, vol. 49, no. 12, pp. 5128–5139, Dec. 2011.

[16] M. Leigsnering, F. Ahmad, M. Amin, and A. Zoubir, "Compressive sensing based specular multipath exploitation for through-the-wall radar imaging," in *IEEE Int. Conf. Acoustics, Speech, and Signal Processing (ICASSP)*, Vancouver, Canada, May 2013, pp. 6004–6008.

[17] G. Gennarelli, I. Catapano, and F. Soldovieri, "RF/microwave imaging of sparse targets in urban areas," *IEEE Antennas and Wireless Propagation Letters*, vol. 12, pp. 643–646, May 2013.

[18] F. Ahmad and M. G. Amin, "Through-the-wall human motion indication using sparsity-driven change detection," *IEEE Transactions on Geoscience and Remote Sensing*, vol. 51, no. 2, pp. 881–890, Feb. 2013.

[19] N. Onhon and M. Cetin, "A sparsity-driven approach for joint sar imaging and phase error correction," *IEEE Transactions on Image Processing*, vol. 21, no. 4, pp. 2075–2088, April 2012.

[20] S.-J. Wei, X.-L. Zhang, and J. Shi, "An autofocus approach for model error correction in compressed sensing SAR imaging," in *IEEE International Geoscience and Remote Sensing Symposium (IGARSS)*, Munich, Germany, Jul. 2012, pp. 3987–3990.

[21] J. Yang, X. Huang, J. Thompson, T. Jin, and Z. Zhou, "Compressed sensing radar imaging with compensation of observation position error," *IEEE Transactions on Geoscience and Remote Sensing*, vol. 52, no. 8, pp. 4608–4620, Aug. 2014.

[22] Y. Yu, A. Petropulu, and H. Poor, "CSSF MIMO radar: Compressive-sensing and step-frequency based MIMO radar," *IEEE Transactions on Aerospace and Electronic Systems*, vol. 48, no. 2, pp. 1490–1504, Apr. 2012.

[23] B. Li and A. Petropulu, "Efficient target estimation in distributed MIMO radar via the ADMM," in *48th Annual Conference on Information Sciences and Systems (CISS)*. IEEE, 2014, pp. 1–5.

[24] F. Ahmad and M. Amin, "Partially sparse reconstruction of behind-the-wall scenes," in *Proceedings SPIE Symposium on Defense, Security, and Sensing, Compressive Sensing Conference*, vol. 8365, Baltimore, USA, April 2012.

[25] E. Lagunas, M. G. Amin, F. Ahmad, and M. Nájar, "Joint wall mitigation and compressive sensing for indoor image reconstruction," *IEEE Transactions on Geoscience and Remote Sensing*, vol. 51, no. 2, pp. 891–906, Feb. 2013.

[26] F. Ahmad, J. Qian, and M. Amin, "Wall clutter mitigation using discrete prolate spheroidal sequences for sparse reconstruction of indoor stationary scenes," *IEEE Transactions on Geoscience and Remote Sensing*, vol. 53, no. 3, pp. 1549–1557, Mar. 2015.

[27] M. Leigsnering, F. Ahmad, M. Amin, and A. Zoubir, "CS based specular multipath exploitation in TWRI under wall position uncertainties," in *IEEE Sensor Array and Multichannel Signal Processing Workshop (SAM)*, A Coruña, Spain, Jun. 2014, pp. 481–484.

[28] A. Gurbuz, J. McClellan, and W. Scott, "Compressive sensing for subsurface imaging using ground penetrating radar," *Signal Processing*, vol. 89, no. 10, pp. 1959–1972, Oct. 2009.

[29] J. Qian, F. Ahmad, and M. G. Amin, "Joint localization of stationary and moving targets behind walls using sparse scene recovery," *Journal of Electronic Imaging*, vol. 22, no. 2, p. 021002, Jun. 2013.

[30] J. Tropp, "Greed is good: algorithmic results for sparse approximation," *IEEE Transactions on Information Theory*, vol. 50, no. 10, pp. 2231–2242, Oct. 2004.

[31] Y. Eldar, P. Kuppinger, and H. Bolcskei, "Block-sparse signals: Uncertainty relations and efficient recovery," *IEEE Transactions on Signal Processing*, vol. 58, no. 6, pp. 3042–3054, Jun. 2010.

[32] L. Potter, E. Ertin, J. Parker, and M. Cetin, "Sparsity and compressed sensing in radar imaging," *Proceedings of the IEEE*, vol. 98, no. 6, pp. 1006–1020, june 2010.

[33] D. Donoho and M. Elad, "Optimally sparse representation in general (nonorthogonal) dictionaries via ℓ_1 minimization," *Proceedings of the National Academy of Sciences*, vol. 100, no. 5, pp. 2197–2202, 2003.

[34] S. Wright, R. Nowak, and M. Figueiredo, "Sparse reconstruction by separable approximation," *IEEE Transactions on Signal Processing*, vol. 57, no. 7, pp. 2479–2493, Jul. 2009.

[35] R. Baraniuk, V. Cevher, M. Duarte, and C. Hegde, "Model-based compressive sensing," *IEEE Transactions on Information Theory*, vol. 56, pp. 1982–2001, Apr. 2010.

[36] E. Lagunas, M. G. Amin, F. Ahmad, and M. Nájar, "Determining building interior structures using compressive sensing," *Journal of Electronic Imaging*, vol. 22, no. 2, pp. 021 003–021 003, 2013.

[37] F. Ahmad and M. Amin, "Multi-location wideband synthetic aperture imaging for urban sensing applications," *Journal of the Franklin Institute*, vol. 345, no. 6, pp. 618–639, Sep. 2008.

[38] S. Boyd and L. Vandenberghe, *Convex Optimization*. New York, NY: Cambridge University Press, Mar. 2004.

[39] P. E. Gill, W. Murray, and M. H. Wright, *Practical optimization*. London, UK: Academic Press, 1981.

[40] J. Kennedy and R. Eberhart, "Particle swarm optimization," in *Proceedings of IEEE International Conference on Neural Networks*, vol. 4, Perth, Australia, Nov. 1995, pp. 1942–1948.

[41] R. Poli, J. Kennedy, and T. Blackwell, "Particle swarm optimization," *Swarm Intelligence*, vol. 1, no. 1, pp. 33–57, Aug. 2007.

[42] E. Baranoski, "Visibuilding: Sensing through walls," in *IEEE Workshop on Sensor Array and Multichannel Processing (SAM)*, Jul. 2006, pp. 1–22.

[43] S. Chen, "Another particle swarm toolbox (http://www.mathworks.com/matlabcentral/fileexchange/25986)," MATLAB Central File Exchange, 2009–14, retrieved April 1st 2014.

[44] Y. Rubner, C. Tomasi, and L. J. Guibas, "The earth mover's distance as a metric for image retrieval," *International Journal of Computer Vision*, vol. 40, no. 2, pp. 99–121, Nov. 2000.

[45] O. Pele and M. Werman, "Fast and robust earth mover's distances," in *IEEE 12th International Conference on Computer Vision*, Kyoto, Japan, Sep. 2009, pp. 460–467.

[46] F. Ahmad and M. Amin, "Wall clutter mitigation for MIMO radar configurations in urban sensing," in *11th International Conference on Information Science, Signal Processing and their Applications (ISSPA)*, Montreal, Canada, Jul. 2012, pp. 1165–1170.